Letters

A Dual-Objective Magnetic Integration-Based WPT Link for UAV Hover Charging With High-Resolution Dynamic Position Detection

Changsong Cai, *Senior Member, IEEE*, Yinfeng Du, Junhua Wang, *Member, IEEE*, Yufeng Jiang, Zhaoyang Yuan, *Member, IEEE*, Xian Zhang, Leke Wan, and Xi Wu

***Abstract*—Hovering wireless power transfer (WPT) helps uncrewed aerial vehicles (UAVs) to achieve flexible and reliable charging, in which the position detection of the energy pickup receiver is crucial for practical applications. In this letter, a dual-objective magnetic integration based WPT link is proposed for dynamic detection and hovering charging of UAVs. Two pairs of orthogonal windings are integrated into the transmitter side, serving both as a step-down inductor and for high-resolution position detection of the receiver. A corresponding position detection strategy based on a simple voltage/current sensing and coupling mapping mechanism is implemented. An experimental prototype is established and the results demonstrate the effectiveness of this approach.**

***Index Terms*—Dual-objective magnetic integration, receiver position detection, uncrewed aerial vehicles (UAVs) hover charging, wireless power transfer (WPT).**

I. Introduction

UNCREWED aerial vehicles (UAVs) have been widely used in resource exploration, terrain detection, and power inspection due to their many advantages, such as simple structure, lower cost, and adaptability [1]. However, due to the limited energy storage capacity, UAVs encounter the bottleneck of frequent charging and insufficient working range [2]. Wireless power transfer (WPT) technology has emerged as a promising solution for recharging UAVs, which can power on-board batteries without physical connection [3].

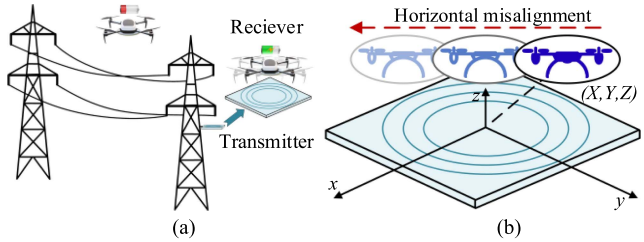

Fig. 1. Schematic of wireless charging for a hovering UAV. (a) Typical application scenario. (b) Charging platform.

In previous studies, a number of efforts have been made to improve the performance of WPT solutions for UAVs, such as airgap distance, power, efficiency, and misalignment tolerance [4], [5], [6], [7]. However, the above schemes all require the UAV to land on the energy transmitter (Tx) platform for charging. Due to the flight controller and motors being turned OFF, safe and stable energy supplement cannot be ensured under complex environments, such as strong winds. Especially considering the scenarios of long-time and large-area operation, repeated takeoffs and landings of the UAV will inevitably reduce the operation efficiency. Therefore, hovering charging of UAVs, as shown in Fig. 1, which can realize uninterrupted operation and ensure reliable charging, is an encouraging alternative to landed charging technology [8].

The misalignment of receiver (Rx) and Tx may occur during UAV hover charging due to environmental disturbances, which may interfere with the transmission performance of the WPT system. Therefore, realizing dynamic position detection of the Rx is crucial for practical applications of UAV hover charging. The prior references used GPS, antenna arrays, tunnel magneto resistance (TMR) sensors, and ultrasonic sensors to detect the position of the Rx, but these methods may be interfered by the environment and are costly to implement [9], [10]. To address this issue, the electromagnetic characteristics of the WPT system are being studied in order to utilize the electric parameters to detect the Rx. Multiple auxiliary localization coils are placed at the Rx side [11], where the position of the Rx is obtained by

Received 6 March 2025; revised 13 April 2025; accepted 1 May 2025. Date of publication 12 May 2025; date of current version 5 August 2025. This work was supported in part by the National Natural Science Foundation of China under Grant 52207013 and Grant U24A20144, in part by the State Key Laboratory of Reliability and Intelligence of Electrical Equipment under Grant EERI_KF2023003, in part by the Hebei University of Technology, in part by S&T Program of Hebei under Grant 225676163GH, and in part by the Hubei Provincial Natural Science Foundation of China under Grant 2024AFB745. *(Corresponding author: Junhua Wang.)*

Changsong Cai, Yinfeng Du, Junhua Wang, Yufeng Jiang, Zhaoyang Yuan, Leke Wan, and Xi Wu are with the Hubei Key Laboratory of Power Equipment and System Security for Integrated Energy, School of Electrical Engineering and Automation, Wuhan University, Wuhan 430072, China, and also with the School of Electrical Engineering and Automation, Wuhan University, Wuhan 430072, China (e-mail: changsongcai@whu.edu.cn; yinfengdu@whu.edu.cn; junhuawang@whu.edu.cn; 2023102070029@whu.edu.cn; zyyuan@ieee.org; lekewan@whu.edu.cn; wu_xii@whu.edu.cn).

Xian Zhang is with the State Key Laboratory of Reliability and Intelligence of Electrical Equipment, Hebei University of Technology, Tianjin 300401, China (e-mail: zhangxian@hebut.edu.cn).

Color versions of one or more figures in this article are available at https://doi.org/10.1109/TPEL.2025.3569069.

Digital Object Identifier 10.1109/TPEL.2025.3569069

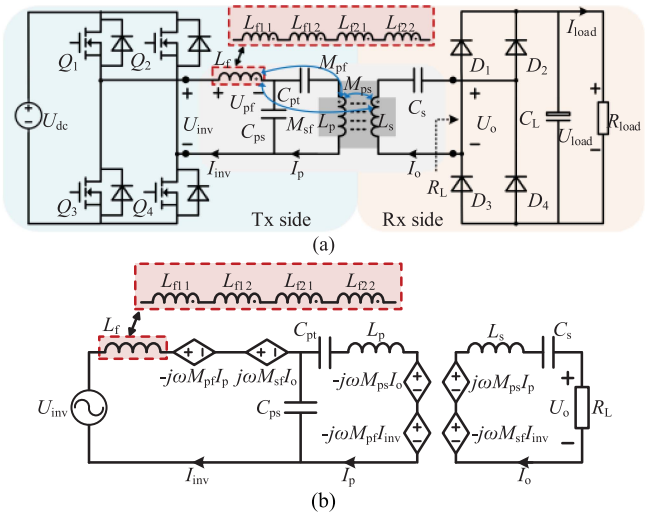

Fig. 2. Circuit diagram of dual-objective magnetic integration topology. (a) Circuit diagram. (b) Equivalent circuit model.

detecting the voltage induced by each auxiliary coil. However, the array of auxiliary coils increases the Rx burden and is not applicable to UAVs. A method for Rx position detection using coil voltage pulses on the Tx side is proposed in [12]. The presented detection method avoids increasing the weight of the UAV, but can only detect a single direction and cannot localize the Rx position coordinates. Therefore, it is urgent to develop a cost-effective Rx position detection method with a compact coupler structure, which is also suitable for UAV hover charging.

In this letter, a dual-objective magnetic integration based WPT link is proposed for dynamic detection and hovering charging of UAVs. Two pairs of orthogonal windings are integrated on the Tx side to serve as a step-down inductor as well as for Rx position detection. A position detection strategy based on the integrated inductor is proposed to realize high-resolution dynamic detection. The proposed WPT link utilizes the inductor–capacitor—capacitor–series (*LCC*-S) compensation topology, which achieves the magnetic integration of the compensation inductor while retaining the constant voltage output capability.

II. Proposed Magnetic Integration-Based WPT Link

A. System Overview

The proposed WPT link obtains Rx position information through a dual-objective magnetic integration inductor, and corresponding coupling mapping mechanism. Fig. 2(a) presents the circuit diagram of the dual-objective magnetic integration-based WPT link employing *LCC*-S compensation topology. L_{f} represents the integrated inductor coil, which adopts a magnetic integration design. C_{ps} and C_{pt} are the compensation capacitors on the Tx side, and C_{s} is the Rx side compensation capacitor. L_{p} and L_{s} are the inductance of the Tx and Rx coils, respectively. M_{ps}, M_{pf}, and M_{sf} are the mutual inductances (MIs) correlated to the coils, which are represented in the subscript. U_{dc} is the DC input voltage and U_{load} is the load voltage. U_{inv}, U_{f} , and U_{o} are the root mean square (RMS)values of the inverter output voltage, the voltage across L_{f} , and the ac output voltage respectively. I_{inv}, I_{p} , and I_{o} are the rms values of the inverter output current, the current flowing through the Tx coil, and the current flowing through the Rx coil, respectively. I_{load} is the load current. R_{L} is the equivalent load resistance. Through the proposed magnetic integration design, the MI between the integrated inductor coil and the Rx coil can reflect the position of the Rx coil, which is the key to realizing position detection.

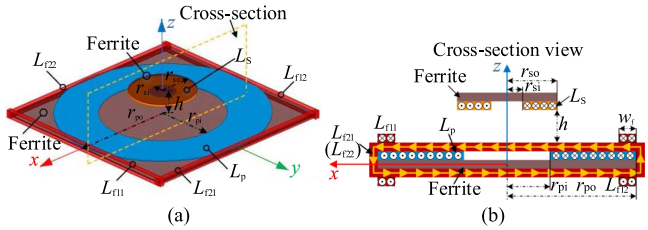

Fig. 3. Proposed coil structure. (a) Oblique view. (b) Cross-section view.

TABLE I
Design Parameters of the Proposed Coil Structure

Parameter	Value	Parameter	Value
r_{po}	240 mm	w_{f}	5 mm
r_{pi}	142 mm	N_{p}	14
r_{so}	76 mm	N_{s}	20
r_{si}	30 mm	N_{f}	4

B. Dual-Objective Integration Design and Basic Performance

The proposed coil structure and cross-section are shown in Fig. 3. In the coupler, asymmetric circular coils are employed as the Tx and Rx coils, and ferrites are mounted behind both coils to enhance the magnetic field coupling. The design focuses on the integrated inductor coil L_{f}. In order to utilize the electromagnetic characteristics of the WPT to simultaneously achieve high-resolution detection of the *x*- and *y*-axes coordinates of the Rx, the integrated inductor coil consists of two pairs of orthogonal windings wound around the edge of the ferrite at the Tx side. The inductances of the four coils, i. e., L_{f11}, L_{f12}, L_{f21}, and L_{f22}, are equal to each other. With the orthogonal structure shown in Fig. 3(a), the two pairs of coils, (L_{f11}, L_{f12}) and (L_{f21}, L_{f22}), are decoupled from each other, and the *x*- and *y*-axes coordinates of the Rx can be detected independently. In addition, to eliminate the cross-coupling between the integrated inductor coil and the Tx coil, two pairs of orthogonal windings are connected in series with the same polarity and the current directions are shown in Fig. 3(b). The crucial design parameters of the proposed coil structure are listed in Table I, where N_{p}, N_{s}, and N_{f} are the number of coil turns.

The proposed dual-objective magnetic integration involves multiple MIs, some of these are crucial for Rx detection. As shown in Fig. 4, $M_{\mathrm{f11\text{-}12}}$, $M_{\mathrm{f11\text{-}21}}$, and $M_{\mathrm{f11\text{-}22}}$ are the MIs between L_{f11} and L_{f12}, L_{f21}, and L_{f22}, respectively. $M_{\mathrm{f11\text{-}p}}$ and $M_{\mathrm{f11\text{-}s}}$ are the MIs between L_{f11} and the Tx coil, and between L_{f11} and the Rx coil, respectively. The MIs associated with L_{f12}, L_{f21}, and L_{f22} in the integrated inductor coil relative to the surrounding inductors are comparable. Fig. 5(a) shows the

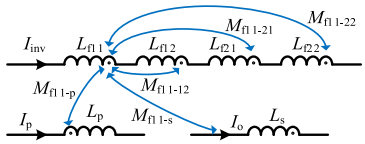

Fig. 4. Schematic diagram of MIs between L_{f11} and the surrounding inductors.

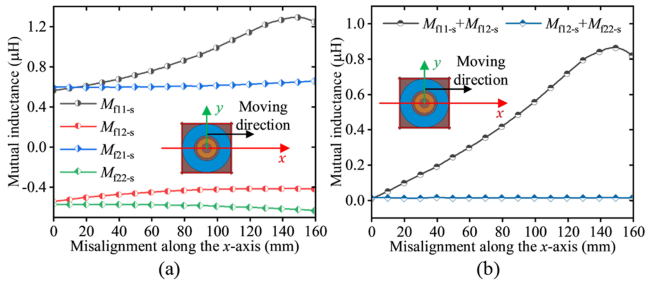

Fig. 5. MIs between the integrated coils and the Rx coil versus the position misalignment along the x-axis. (a) MI of a single coil and the Rx coil. (b) Sum of MI of the opposite coils.

finite element analysis simulation results of the MIs between the four coils in the integrated inductor coil and the Rx coil under different misalignments along the x-axis. Fig. 5(b) shows that ($M_{f11\text{-}s}$+$M_{f12\text{-}s}$) increases and ($M_{f21\text{-}s}$+$M_{f22\text{-}s}$) remains constant when the misalignment is less than 150 mm. Therefore, ($M_{f11\text{-}s}$+$M_{f12\text{-}s}$) and ($M_{f21\text{-}s}$+$M_{f22\text{-}s}$) can be used as mapping indicators for the x- and y-axes coordinates of the Rx, which vary monotonically from −150 to 150 mm and are independent of each other.

As the Rx moves, the MIs will change according to analysis, which is crucial for the dynamic detection of the Rx, but it is necessary to further analyze the effect of magnetic integration on the characteristics of the *LCC*-S topology. When the inductance and capacitance satisfy (1), the circuit is in resonant state, where ω is the resonant angular frequency and f is the resonance frequency. Since the response of the circuit at the fundamental frequency in the resonant state is most significant, the effect of higher harmonics can be neglected. Consequently, the subsequent analysis will be conducted based on fundamental harmonic analysis (FHA), and Fig. 2(b) shows the equivalent circuit model based on FHA.

$$\omega = 2\pi f = 1\Big/\sqrt{L_f C_{ps}} = 1\Big/\sqrt{(L_p - L_f)C_{pt}} = 1\Big/\sqrt{L_s C_s}. \tag{1}$$

Since the integrated inductor coil is decoupled from the Tx coil, M_{pf} can be neglected. According to Kirchhoff's voltage law, the input impedance and $\dot{U}_o$ can be derived as

$$Z_{in} = R_L/(\omega^4 C_{ps}^2 M_{ps}^2) + 2jM_{sf}/(\omega C_{ps} M_{ps}) \tag{2}$$

$$\dot{U}_o = \frac{M_{ps}\dot{U}_{inv}}{L_f}\Bigg/\left(1 + \frac{2j\omega M_{ps}M_{sf}}{L_f R_L}\right). \tag{3}$$

Due to the presence of M_{sf}, the imaginary part of Z_{in} and the existence of R_L in the $\dot{U}_o$ expressions are unavoidable. However, the value of M_{sf} is small. As shown in Fig. 5(b), when Rx is aligned, M_{sf} is close to zero. Even if the misalignment occurs, M_{sf} is less than 1.7 μH. M_{ps} is measured to be about 10 μH. By substituting the parameters from Table II into (2) and (3), the following results are obtained:

$$\begin{cases} \mathrm{Im}(Z_{in})/\mathrm{Re}(Z_{in}) = 2\omega^3 C_{ps} M_{sf} M_{ps}/R_L = 0.1041 \\ 2j\omega M_{ps} M_{sf}/(L_f R_L) = 0.1042. \end{cases} \tag{4}$$

It is found that the effect of M_{sf} on Z_{in} and $\dot{U}_o$ is nearly negligible, thereby having no significant impact on the performance of the proposed WPT link.

TABLE II
PARAMETER VALUES OF THE EXPERIMENTAL PROTOTYPE

Parameter	Value	Parameter	Value
U_{dc}	150 V	L_{f21}	10.35 μH
f	300 kHz	L_{f22}	10.15 μH
L_p	174.5 μH	C_{ps}	6.86 nF
L_s	67.3 μH	C_{pt}	2.11 nF
L_f	41 μH	C_s	4.18 μH
L_{f11}	10.18 μH	U_{dc}	150 V
L_{f12}	10.38 μH	R_{load}	15 Ω

C. Dynamic Position Detection Strategy

Based on the dual-objective magnetic integration design, three mapping indicators are proposed to derive the position information of the Rx. These indicators leverage the characteristics of the MIs between the Rx coil and other coils, and the Rx detection flow is comprehensively described in conjunction with the mapping indicators.

According to Fig. 4, the voltage $\dot{U}_{Lf11}$ across L_{f11} is

$$\dot{U}_{Lf11} = j\omega L_{f11}\dot{I}_{inv} + j\omega(M_{f11-12} + M_{f11-21} + M_{f11-22})\dot{I}_{inv} - j\omega M_{f11-p}\dot{I}_p + j\omega M_{f11-s}\dot{I}_o. \tag{5}$$

Similarly, the voltage $\dot{U}_{Lf12}$ across L_{f12} is

$$\dot{U}_{Lf12} = j\omega L_{f12}\dot{I}_{inv} + j\omega(M_{f12-11} + M_{f12-21} + M_{f12-22})\dot{I}_{inv} - j\omega M_{f12-p}\dot{I}_p + j\omega M_{f12-s}\dot{I}_o \tag{6}$$

where $M_{f12\text{-}11}$, $M_{f12\text{-}21}$, $M_{f12\text{-}22}$, $M_{f12\text{-}p}$, and $M_{f12\text{-}s}$ are the MIs between L_{f12} and L_{f11}, L_{f21}, L_{f22}, the Tx coil, and the Rx coil, respectively. Since the Tx of the proposed coupler has a symmetric structure, combined with the direction of the magnetic field generated by the current shown in Fig. 3(b), it can be deduced that

$$\begin{cases} M_{f11-12} = M_{f12-11} \\ M_{f11-p} = -M_{f12-p} \\ M_{f11-21} = -M_{f11-22} = M_{f12-22} = -M_{f12-21}. \end{cases} \tag{7}$$

Summing (5) and (6) and substituting into (7) yields

$$F_x = (\dot{U}_{Lf11} + \dot{U}_{Lf12} - j\omega(L_{f11} + L_{f12} + 2M_{f11-12})\dot{I}_{inv})\Big/\dot{I}_o = j\omega(M_{f11-s} + M_{f12-s}) \tag{8}$$

where F_x is defined as a mapping indicator for realizing x-direction position detection, and its value is solely related to

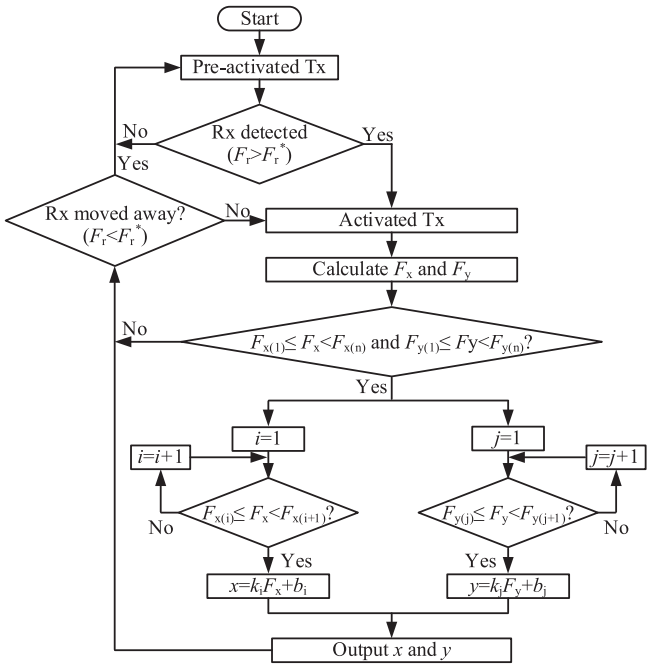

Fig. 6. Flowchart of the Rx position detection.

$(M_{f11\text{-}s}+M_{f12\text{-}s})$. Similarly, the mapping indicator F_y can be constructed to estimate the position in the y-direction

$$F_y = (\dot{U}_{Lf21}+\dot{U}_{Lf22} - j\omega(L_{f21}+L_{f22}+2M_{f21-22})\dot{I}_{inv}) \Big/ \dot{I}_o = j\omega(M_{f21-s} + M_{f22-s}). \quad (9)$$

Since the monotonicity of F_x and F_y reverses when the misalignment exceeds 150 mm, an auxiliary indicator F_r is constructed according to (3) in order to help determine whether the Rx is within the recognizable range

$$F_r = \frac{\dot{U}_o L_f}{\dot{U}_{inv} - 2j\omega M_{sf}\dot{I}_o} = \frac{\dot{U}_o L_f}{\dot{U}_{inv} - 2(F_x + F_y)\dot{I}_o} = M_{ps}. \quad (10)$$

F_r denotes the distance between the Rx and the center of the Tx. When F_r is greater than the preset value F_r^*, it means that the Rx is within the recognizable range. Fig. 6 illustrates the flowchart of the proposed dynamic position detection method. In this flowchart, the Tx is first preactivated at low power and whether the Rx enters the recognizable range is determined by comparing F_r with a preset value F_r^*. If the Rx is within the recognizable range, the Tx is activated at the rated power. Then, the real-time F_x and F_y are calculated by measuring the target parameters. Finally, F_x and F_y are fed into a prebuild segmented fitting function as shown in (11) to calculate the position coordinates, thus determining the position of the Rx

$$x_i = k_i F_{x(i)} + b_i (i = 1, 2.., n-1)$$
$$\begin{cases} k_i = \frac{x_{i+1}-x_i}{F_{x(i+1)}-F_{x(i)}} \\ b_i = x_i - k_i F_{x(i)}. \end{cases} (i = 1, 2.., n-1) \quad (11)$$

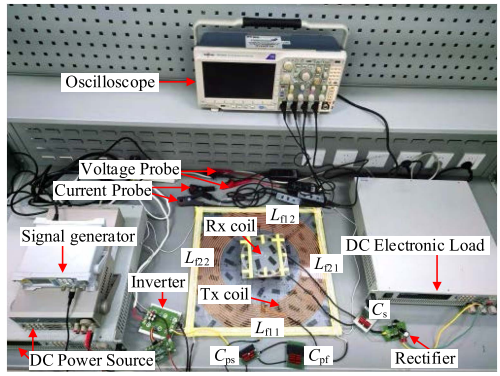

Fig. 7. Established experimental prototype.

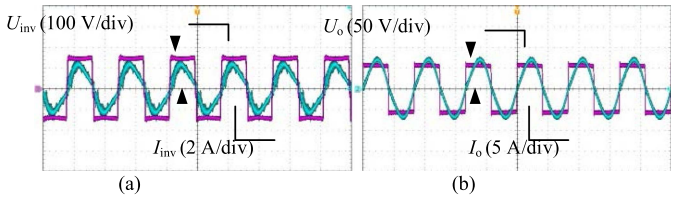

Fig. 8. Experimental waveforms with rated outputs. (a) Inverter output waveform. (b) Rectifier input waveform.

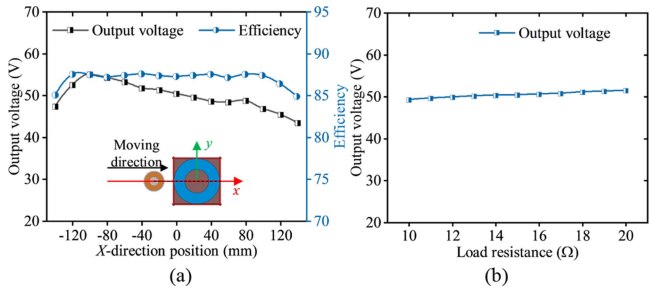

Fig. 9. Experimental results of the prototype. (a) Output voltage and efficiency versus horizontal misalignment. (b) Output voltage versus load resistance.

III. Experimental Verification

In order to verify the proposal, a 245 W experimental prototype operating at 300 kHz is built, as shown in Fig. 7. The experimental parameters are shown in Table II. Fig. 8 shows the experimental waveforms at the rated power of the system. Fig. 8(a) depicts the output of the inverter and Fig. 8(b) illustrates the input of the rectifier. It is observed that the zero voltage switch (ZVS) of the inverter is essentially achieved.

The output voltage and dc–dc efficiency against the horizontal misalignment are measured, as shown in Fig. 9(a). The dc–dc efficiency of the established experimental prototype maintains above 87% as the horizontal misalignment varies from −100 to 100 mm, exhibiting a relatively stabilized antimisalignment performance. Fig. 9(b) shows the output voltage versus load resistance of the experimental prototype. When the load resistance is changed from 10 to 20 Ω, the output voltage varies from 49.2 to 51.4 V. Therefore, the experimental prototype has constant voltage output capability.

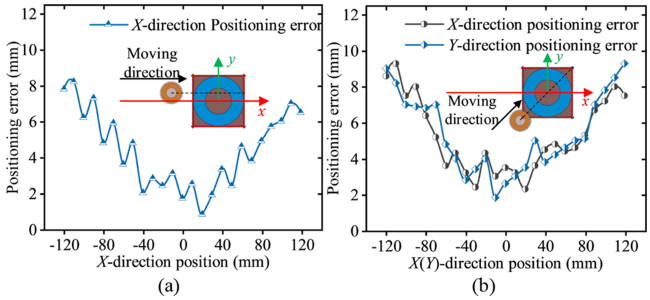

Fig. 10. Position detection error. (a) Rx moves axially along $y = 80$ mm through the Tx. (b) Rx moves diagonally along $y = x$ through the Tx.

TABLE III
COMPARISONS WITH PREVIOUS RX DETECTION METHODS

References	Method	Overall cost	Volume and weight	Positioning error
[11]	Additional detection coils	★★	★	30 mm
[12]	voltage pulses detection	★★★	★★★	No coordinate position
This work	Dual-objective magnetic integration	★★★	★★★	10 mm

The number of "★" represents the performance.

To verify the proposed high-resolution dynamic position detection strategy for UAVs based on dual-objective magnetic integration, two typical scenarios of UAV hover charging are selected, specifically testing the positioning errors when the Rx coil passes through the Tx along the axial and diagonal directions, respectively, as shown in Fig. 10. The positioning errors are calculated by (12), where (x_e, y_e) and (x_a, y_a) are the estimated and actual values of the Rx position coordinates, respectively. Experimental results show that the positioning errors in both scenarios are between $[-10$ mm, 10 mm$]$ when the Rx coil is within the recognizable range, making it suitable for dynamic position detection of UAV hover charging

$$e_x = |x_e - x_a|, e_y = |y_e - y_a|. \tag{12}$$

To highlight the advantages of the proposal, current UAV position detection methods are compared and analyzed in terms of positioning method, overall cost, volume and weight, and positioning error in Table III. According to the comparison, the proposal in this letter is more practical, cost-effective, lighter in weight, and offers more accurate in positioning.

IV. CONCLUSION

In this letter, a dual-objective magnetic integration-based WPT link is proposed for UAV hover charging. By integrating two pairs of orthogonal windings, three mapping indicators are constructed to achieve high-resolution dynamic position detection during UAV hover charging. Moreover, the proposed WPT link maintains the load-independent constant voltage output characteristic. A 245 W WPT experimental prototype is built to verify the proposed position detection strategy. The experimental results show that the positioning errors are relatively small when the Rx moves axially and diagonally within the recognizable range, and the output voltage barely fluctuates when the load resistance is changed.

REFERENCES

[1] T. Long, M. Ozger, O. Cetinkaya, and O. B. Akan, "Energy neutral Internet of Drones," *IEEE Commun. Mag.*, vol. 56, no. 1, pp. 22–28, Jan. 2018.
[2] W. Han, K. T. Chau, C. Jiang, W. Liu, and W. H. Lam, "Design and analysis of quasi-omnidirectional dynamic wireless power transfer for fly-and-charge," *IEEE Trans. Magn.*, vol. 55, no. 7, Jul. 2019, Art. no. 8001709.
[3] Z. Zhang, H. Pang, A. Georgiadis, and C. Cecati, "Wireless power transfer—An overview," *IEEE Trans. Ind. Electron.*, vol. 66, no. 2, pp. 1044–1058, Feb. 2019.
[4] C. Song et al., "EMI reduction methods in wireless power transfer system for drone electrical charger using tightly coupled three-phase resonant magnetic field," *IEEE Trans. Ind. Electron.*, vol. 65, no. 9, pp. 6839–6849, Sep. 2018.
[5] C. Cai, J. Wang, H. Nie, P. Zhang, Z. Lin, and Y. Zhou, "Effective configuration WPT systems for drones charging area extension featuring quasi-uniform magnetic coupling," *IEEE Trans. Transp. Electrific.*, vol. 6, no. 3, pp. 920–934, Sep. 2020.
[6] Y. Li et al., "A new magnetic coupler with high rotational misalignment tolerance for unmanned aerial vehicles wireless charging," *IEEE Trans. Power Electron.*, vol. 37, no. 11, pp. 12986–12991, Nov. 2022.
[7] J. Wang, R. Chen, C. Cai, J. Zhang, and C. Wang, "An onboard magnetic integration based WPT system for UAV misalignment-tolerant charging with constant current output," *IEEE Trans. Transp. Electrific.*, vol. 9, no. 1, pp. 1973–1984, Mar. 2023.
[8] K. Chen and Z. Zhang, "In-flight wireless charging: A promising application-oriented charging technique for drones," *IEEE Ind. Electron. Mag.*, vol. 18, no. 1, pp. 6–16, Mar. 2024.
[9] J. Li, F. Yin, L. Wang, B. Cui, and D. Yang, "Electromagnetic induction position sensor applied to anti-misalignment wireless charging for UAVs," *IEEE Sensors J.*, vol. 20, no. 1, pp. 515–524, Jan. 2020.
[10] J. T. Vaheeda and B. George, "TMR sensor-based detection of EVs in semi-dynamic traffic for optimal charging," *IEEE Trans. Intell. Transp. Syst.*, vol. 23, no. 8, pp. 13721–13730, Aug. 2022.
[11] L. Tan et al., "Mesh-based accurate positioning strategy of EV wireless charging coil with detection coils," *IEEE Trans. Ind. Informat.*, vol. 17, no. 5, pp. 3176–3185, May 2021.
[12] S. Nagai, Y. Satoh, K. Fujimoto, and H. Fujimoto, "Sensorless drone detection for in-flight inductive power transfer using transmitter-side voltage pulses," in *Proc. IEEE Wireless Power Technol. Conf. Expo*, 2024. pp. 557–561.